Research Square

Preprints are preliminary reports that have not undergone peer review.
They should not be considered conclusive, used to inform clinical practice,
or referenced by the media as validated information.

Assessing Cyclonic Changes in Mangrove Dynamics with Multispectral to Continuous Hyperspectral Transformation

Souherdya Sarkar
Institute of Engineering and Management, Kolkata
Swarnalee Ray
Institute of Engineering and Management, Kolkata
Anindita Das Bhattacharjee
anindita.dasbhattacharjee@iem.edu.in
Institute of Engineering and Management, Kolkata

Research Article

Keywords: Mangrove, change detection, Cyclone, Sentinel-2, Reconstruction

Posted Date: November 11th, 2026

DOI: https://doi.org/10.21203/rs.3.rs-11270315/v1

License: This work is licensed under a Creative Commons Attribution 4.0 International License.
Read Full License

Additional Declarations: No competing interests reported.

Assessing Cyclonic Changes in Mangrove Dynamics with Multispectral to Continuous Hyperspectral Transformation

Souherdya Sarkar[1], Swarnalee Ray[1], Anindita Das Bhattacharjee[1*]

[1] Institute of Engineering and Management (IEM), University of Engineering and Management Kolkata, IEM Centre of Excellence for InnovAI, Department of Computer Science & Engineering, Kolkata, 700091, West Bengal, India .

*Corresponding author(s). E-mail(s): anindita.dasbhattacharjee@iem.edu.in;
Contributing authors: souherdya.sarkar@iem.edu.in; swarnalee.ray@iem.edu.in;

Abstract

The limited spectral resolution of available multispectral satellite imagery restricts the research to assessing cyclone-induced mangrove degradation. The eight vegetation-sensitive Sentinel-2 bands cannot continuously resolve the green-to-red, red-edge, and near-infrared regions. Therefore, canopy stress, chlorophyll loss, moisture alteration, fragmentation, and subsequent recovery from multispectral images become difficult. This study proposes Ecologically Bounded Spectral Reconstruction using Multi-Regime Interpolation (EBSR-MR). This algorithm aims to transform eight Sentinel-2 surface-reflectance bands into a continuous 101-band hyperspectral representation spanning 400–900 nm. The methodological innovation focuses on wavelength-specific reconstruction regimes, preservation of measured Sentinel-2 bands as spectral anchors, Gaussian modeling of the nonlinear red-edge transition, smooth boundary integration between spectral regimes, and ecologically constrained visible and near-infrared interpolation. These components are needed to reconstruct a reflectance curve that follows the expected physical behavior of real mangrove vegetation. This will prevent physically implausible reflectance behavior and help in reconstructing diagnostically important wavelengths absent from the native sensor. EBSR-MR was evaluated over the cyclone-affected mangroves (pre-Amphan (2019), post-Amphan (2021), and recovery-stage (2023) of Henry Island, Indian Sundarbans.EBSR-MR bridges

the spectral gap between accessible multi-spectral imagery and costly hyper-spectral observations by maintaining near-perfect spectral–spatial fidelity. Also, EBSR-MR provides detailed information in the chlorophyll-sensitive red-edge region and estimates the missing 900-nm reflectance needed to identify mangrove canopy moisture, stress, cyclone damage, and recovery more accurately. EBSR-MR is sensor-accessible and does not require adversarial training or extensive labelled samples; it can be adapted for monitoring vegetation responses to floods, droughts, wildfire, and coastal erosion.

Keywords: Mangrove, change detection, Cyclone, Sentinel-2, Reconstruction

1 Introduction

Mangroves are continuously exposed to sea-level rise, coastal erosion, salinity changes, anthropogenic pressure, and tropical cyclones. The mangrove ecosystem and its location at the land–ocean interface make it sensitive to extreme wind, tidal inundation, and storm-surge disturbance. Better spatial coverage and temporal consistency are needed to identify damaged areas, quantify ecosystem recovery, and support conservation and restoration planning Kuenzer et al. (2011); Wang et al. (2019); Sunkur et al. (2024).
Cyclones can alter mangrove ecosystems through defoliation, stem breakage, uprooting, and prolonged inundation, producing both immediate and gradually evolving changes in canopy greenness, chlorophyll concentration, leaf area, moisture condition, and structural connectivity. These spatially heterogeneous effects are exposed to cyclone intensity, wind direction, storm-surge exposure, shoreline configuration, species composition, and pre-existing canopy condition. Satellite-based change detection has been widely used to monitor these disturbances McCarthy et al. (2020).
This study demonstrated the value of high-resolution time-series mapping for identifying mangrove damage and recovery following Hurricane Irma McCarthy et al. (2020). Mondal et al. (2022) combined radar and optical remote sensing to support near-real-time assessment of Cyclone Amphan's effects on mangroves. Bhargava and Friess (2022) further showed that previous shoreline dynamics influenced the future susceptibility of Sundarbans mangroves.
The spectral information available from Sentinel-2 remains discrete and incomplete. The reason is that, although red-edge bands are included, the sensor measures reflectance only at selected band centers separated by unobserved wavelength intervals. The transition between the green and red wavelengths and the nonlinear rise from red absorption to near-infrared reflectance are represented by only a small number of bands. Minute variations occurring between these measured wavelengths may therefore remain unobserved.
Delegido et al. (2011) demonstrated the need for red-edge bands for estimating green leaf area index and chlorophyll content estimation. The reason is Red-edge position, magnitude and slope are sensitive to chlorophyll concentration, leaf area and vegetation stress.
A small number of separated red-edge measurements cannot represent the complete

shape and curvature of the transition, depicted in Frampton et al. (2013). Hyperspectral data addresses this limitation by observing reflectance in numerous narrow and approximately contiguous wavelength bands. Hyperspectral observations provide a more complete representation of absorption features and red-edge behavior when compared with multispectral images. Lassalle et al. (2023) reported that hyperspectral imagery substantially improves mangrove-species discrimination. This study showed greater spectral detail present in hyperspectral images and their ability to identify subtle differences that may remain concealed within broad multispectral bands. The value of narrow-band spectral information in hyperspectral imagery for better resolving the identification of heterogeneous mangrove communities is established in Zhang et al. (2024). Therefore, it is evident that the hyperspectral information is not limited to species classification. Despite these benefits, routine acquisition of satellite hyperspectral data remains constrained by their cost and availability. Directly measured hyperspectral imagery may not provide a consistent multi-temporal record. However, this information is needed to study the complete disturbance–recovery trajectory. Sentinel-2 provides a globally available archive with frequent observations, therefore creating a need for methods that can extract a denser and ecologically meaningful spectral representation from accessible multi-spectral data.

Spectral reconstruction is one of the possible solutions for estimating reflectance at unobserved wavelengths from the available multi-spectral measurements. In remote sensing, hyperspectral reconstruction and multi-spectral–hyperspectral fusion have been implemented using component substitution, matrix factorization, tensor decomposition, and deep neural networks Yokoya et al. (2017). Deep convolutional approaches learn high-spectral-resolution representations while attempting to preserve spatial and spectral consistency Hu et al. (2022). Spatial–spectral prior networks similarly use spectral correlation and spatial structure as reconstruction constraints Jiang et al. (2020). All these studies incorporate advanced hyperspectral super-resolution; many were designed primarily for fusing a low-spatial-resolution hyperspectral image with a high-spatial-resolution multi-spectral image. Therefore, it is evident from all these studies that they need paired multi-spectral–hyperspectral observations, external hyperspectral references, and large training datasets. These requirements limit their application for cyclone events and data-scarce mangrove regions. To address this problem, the present study proposes the Ecologically Bounded Spectral Reconstruction with Multi-Regime Interpolation (EBSR-MR) algorithm. Since mangrove reflectance does not vary uniformly across wavelengths, this algorithm is designed to transform eight vegetation-sensitive Sentinel-2 surface-reflectance bands into a 101-band, hyperspectral-like representation spanning 400–900 nm. The reconstructed spectra are evaluated using Peak Signal-to-Noise Ratio (PSNR), Structural Similarity Index Measure (SSIM), Mean Absolute Error (MAE), Root-Mean-Square Error (RMSE) and Spectral Angle Mapper (SAM).

2 Related Work

Hyperspectral reconstruction aims to recover spectrally dense information primarily from observations with limited spatial or spectral resolution Yokoya et al. (2017). Yokoya et al. (2017) reviewed the principal hyperspectral–multispectral fusion methods

and found that all these approaches combine a high-spatial-resolution multispectral image with a spectrally detailed but spatially coarse hyperspectral image. These methods aim to generate an image with both high spatial and spectral resolution, assuming the presence of a hyperspectral observation. However, hyperspectral imagery is rarely available for the exact pre-disturbance or immediate post-disturbance periods for mangrove ecosystems. EBSR-MR addresses this operational limitation and reconstructs dense spectral representations directly from a single Sentinel-2 acquisition without requiring a contemporaneous hyperspectral image. Akhtar et al. (2014) proposed a sparse spatio-spectral representation which can learn sparse relationships between spectral and spatial information to reconstruct a high-resolution hyperspectral image. However, this approach is suitable only when corresponding high- and low-resolution observations are available.

The outcomes of these methods are dependent on dictionary quality, representation assumptions, and the availability of appropriate reference information. The proposed EBSR-MR does not require dictionary learning or paired high-resolution hyperspectral samples.

Jiang et al. (2020) introduced a spatial–spectral prior network for spatial residual learning, spectral attention, and progressive reconstruction. Hu et al. (2022) developed a deep spatiospectral attention convolutional neural network with nonlinear reconstruction capability. Among the spectral channels, this algorithm can learn spatial correlations and dependencies among spectral channels. However, these algorithms are found to have dependencies on sensor characteristics, atmospheric conditions, land-cover composition, and geographical regions, making them unsuitable for data-scarce mangrove ecosystems.

The proposed EBSR-MR performs spectral densification while retaining the native spatial resolution and observed Sentinel-2 reflectance values. This algorithm expands eight vegetation-sensitive Sentinel-2 bands into a 101-band hyperspectral-like representation covering 400–900 nm. The aim of this proposed algorithm is to generate directly measured hyperspectral information, and it can estimate a continuous spectral representation constrained by the available satellite observations.

Lassalle et al. (2023) reported that narrow and contiguous spectral bands improve mangrove-species discrimination. Undrajavarapu and Sekhar (2020) applied hyperspectral data to identify mangrove species and ecological characteristics. Mangrove reflectance is strongly nonlinear across these regimes; therefore, all the generic reconstruction methods often fail. The reason is that they optimize global statistical error without explicitly accounting for the different physical behaviors of vegetation across the visible, red-edge, and near-infrared regions. Applying a single interpolation function across the complete spectrum may over-smooth the red edge, since visible reflectance is predominantly influenced by pigment absorption, the red edge contains a rapid chlorophyll-sensitive transition, and near-infrared reflectance. In the proposed algorithm, therefore, the nonlinear red-edge transition is modeled separately using Gaussian-based reconstruction. This architecture makes the reconstruction sensitive to the physical meaning of each spectral region. The proposed algorithm avoids treating all missing

wavelengths as a uniform mathematical interpolation problem. The proposed EBSR-MR bridges this methodological gap by combining the accessibility and temporal availability of Sentinel-2 with a spectrally denser representation.

3 Methodology

The overall processing pipeline, from Sentinel-2 acquisition through spectral reconstruction, validation and mangrove dynamics analysis, is summarized in Fig. 1.

3.1 Study Area and Data Acquisition

Sentinel-2 Level-2A surface-reflectance imagery was acquired for three temporal phases relative to Cyclone Amphan: a pre-cyclone baseline (2019), an immediate post-cyclone acquisition (2021), and a recovery-phase acquisition (2023). Eight spectral bands spanning the visible, red-edge, and near-infrared regions were retained for analysis (B02, B03, B04, B05, B06, B07, B08, B8A; central wavelengths 490–865 nm), providing native sampling of two red-edge positions (705 nm, 740 nm) and a single broad NIR window.

3.2 Preprocessing

Each scene was masked for cloud, shadow, and invalid-value pixels, clipped to the mangrove area of interest, and co-registered on a common spatial grid. This yielded a quality-controlled 8-band reflectance vector at every valid pixel, forming the input to spectral reconstruction.

3.3 Ecologically-Bounded Spectral Reconstruction (EBSR-MR)

To increase spectral sampling density beyond the native 8 Sentinel-2 bands, an Ecologically-Bounded Spectral Reconstruction algorithm for Mangrove Regimes (EBSR-MR) was developed (Fig. 1). The algorithm reconstructs a continuous reflectance spectrum at 5 nm intervals from 400–900 nm (101 wavelength points) for every pixel, while constraining the reconstruction to remain physically and ecologically consistent with the coarser measured bands.

3.3.1 Basis Representation

Reconstructed spectra were parameterized as a linear combination of 20 smooth Gaussian basis functions $\phi_k(\lambda)$ evenly centered across the 400–900 nm range, each with a width of 1.5× the basis spacing:

$$\hat{R}(\lambda) = \sum_{k=1}^{20} c_k \, \phi_k(\lambda), \qquad \phi_k(\lambda) = \exp\left(-\frac{(\lambda - \mu_k)^2}{2w^2}\right) \tag{1}$$

where c_k are the coefficients to be estimated for each pixel, μ_k the basis centre, and w the basis width. This low-dimensional, smooth basis constrains the solution space and prevents unrealistic high-frequency oscillations in the reconstructed spectrum.

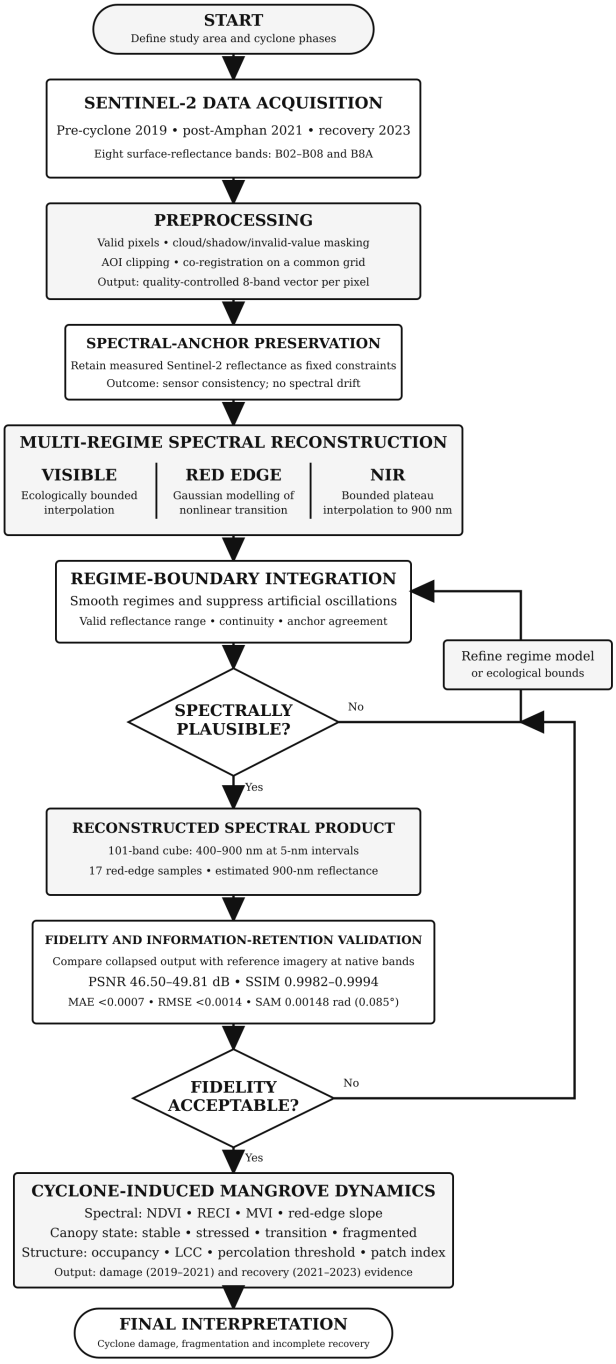


Fig. 1 Workflow of the Ecologically-Bounded Spectral Reconstruction algorithm for Mangrove Regimes (EBSR-MR), from Sentinel-2 data acquisition through multi-regime spectral reconstruction, fidelity validation, and cyclone-induced mangrove dynamics analysis.

3.3.2 Sensor-Consistent Forward Model

To ensure the reconstructed spectrum remained anchored to the actual Sentinel-2 measurements, each candidate spectrum was projected back into Sentinel-2 band space using a Gaussian spectral response function for each band, built from its published central wavelength and full-width bandwidth:

$$S_b(\lambda) = \exp\left(-\frac{(\lambda - \lambda_b)^2}{2\sigma_b^2}\right), \qquad \sigma_b = \frac{\Delta\lambda_b}{2.355} \tag{2}$$

normalised to unit area, where λ_b and $\Delta\lambda_b$ are the centre wavelength and bandwidth of band b. Convolving the reconstructed spectrum with this response matrix simulates the corresponding Sentinel-2 observation, allowing the reconstruction to be evaluated against the true measured reflectance for that pixel (spectral-anchor preservation).

3.3.3 Multi-Regime Reconstruction and Ecological Constraints

Reconstruction was performed jointly across three overlapping spectral regimes reflecting distinct reflectance behaviour in vegetation: the visible region (bounded interpolation informed by expected pigment absorption), the red-edge region (nonlinear transition modelled via the Gaussian basis to increase sampling from 2 native points to 17 points across 680–760 nm), and the NIR region (bounded plateau extrapolation to 900 nm). Basis coefficients c_k were estimated per pixel by minimizing a composite objective function combining three terms:

$$\mathcal{L}(c) = \alpha\,\mathcal{L}_{\text{band}} + \beta\,\mathcal{L}_{\text{smooth}} + \gamma\,\mathcal{L}_{\text{eco}} \tag{3}$$

where $\mathcal{L}_{\text{band}}$ is the mean squared error between the simulated and measured Sentinel-2 reflectance (sensor fidelity), $\mathcal{L}_{\text{smooth}}$ penalizes second-derivative curvature of the reconstructed spectrum (spectral smoothness), and $\mathcal{L}_{\text{eco}}$ is an ecological penalty enforcing known vegetation reflectance behaviour: NIR reflectance exceeding red and green reflectance, a monotonically rising red-edge transition, and reflectance values bounded within the physically valid [0,1] range. Weights were set to $\alpha = 1.0$, $\beta = 0.05$, $\gamma = 0.10$. The objective was minimized using L-BFGS-B with bound constraints, using multiple random restarts per pixel to reduce sensitivity to initialization, with the lowest-loss solution retained.

3.4 Regime-Boundary Integration and Plausibility Check

Reconstructed spectra from the three regimes were integrated into a single continuous 101-band spectral cube per scene, with smoothing applied at regime boundaries to suppress artificial discontinuities. Each reconstructed spectrum was checked for physical plausibility (valid reflectance range, spectral continuity, and agreement with the measured Sentinel-2 anchor bands). Pixels failing this check were returned to the reconstruction stage with refined regime modelling or ecological bounds before re-integration, as shown in the feedback loop of Fig. 1.

3.5 Fidelity and Information-Retention Validation

Reconstruction fidelity was assessed by re-projecting each reconstructed 101-band spectrum back into Sentinel-2 band space using the sensor response matrix and comparing this simulated output against the original measured reflectance at the native 8 bands. Peak Signal-to-Noise Ratio (PSNR), Structural Similarity Index (SSIM), Mean Absolute Error (MAE), Root Mean Square Error (RMSE) and Spectral Angle Mapper (SAM) were computed between simulated and measured band values across all valid pixels (PSNR: 46.50–49.81 dB; SSIM: 0.9982–0.9994; MAE < 0.0007; RMSE < 0.0014; SAM: 0.00148 rad, 0.085°). This validation confirms that the reconstruction is consistent with, and does not distort, the original sensor-measured reflectance; it establishes sensor-domain fidelity rather than independent validation of reflectance values at the unmeasured wavelengths introduced by the reconstruction.

3.6 Cyclone-Induced Mangrove Dynamics

From the validated 101-band reconstructed cubes, spectral indices were computed for each temporal phase (pre-cyclone, post-cyclone, recovery), including the Normalized Difference Vegetation Index (NDVI), the Red-Edge Chlorophyll Index (RECI), the Mangrove Vegetation Index (MVI), and the red-edge slope, calculated from the finely sampled 680–760 nm region. Canopy condition was classified into stable, stressed, transition, and fragmented states, and structural change was characterized using patch-based landscape metrics (occupancy, largest connected component, percolation threshold, patch index). Comparison across phases provided evidence of cyclone-induced damage (2019–2021) and subsequent recovery (2021–2023).

4 Results

4.1 Spectral Reconstruction Output Characterization

The Ecologically-Bounded Spectral Reconstruction via Multi-Regime interpolation (EBSR-MR) algorithm was applied to Sentinel-2 (8-band, 490 nm–865 nm) surface reflectance imagery of Henry Island to generate continuous 101-band hyperspectral reconstructions spanning 400–900 nm. Reconstructions were generated for three temporal phases bracketing Cyclone Amphan (May 2020): a pre-cyclone baseline (2019). An immediate post-cyclone acquisition (2021), and a longer-term recovery acquisition (2023). Before the reconstructed cubes were used for any ecological interpretation, it was necessary to characterize the reconstruction output itself, verifying that the 93 newly synthesized spectral points per pixel are physically plausible, internally consistent with the original Sentinel-2 measurements, and free of artificial noise. This subsection presents that characterization, prior to the fidelity validation (Section 4.2) and downstream ecological analyses (Sections 4.3–4.4).

4.1.1 Before-vs-After Spectral Profiles

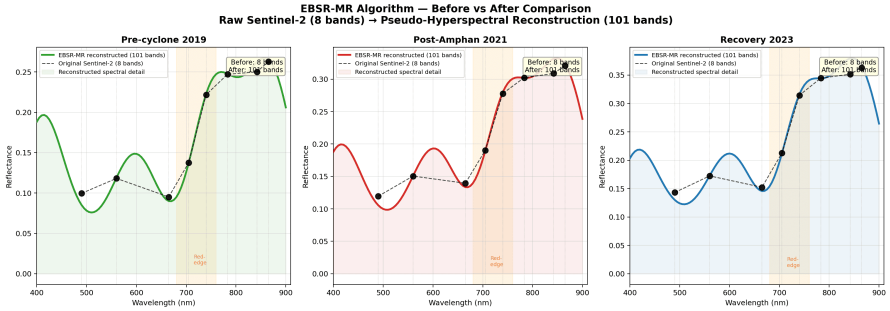


Fig. 2 Comparative spectral reflectance profile of the original 8-band Sentinel-2 measurements (discrete markers) against the reconstructed 101-band EBSR-MR spectrum (continuous curve) for a representative mangrove canopy pixel, Henry Island.

Fig. 2 presents a comparative spectral profile of the original 8-band Sentinel-2 reflectance values against the reconstructed 101-band EBSR-MR output for a representative mangrove canopy pixel. The reconstructed spectrum forms a smooth, continuous curve across the visible-to-near-infrared range, in contrast to the discrete, widely spaced band values of the native Sentinel-2 product. The most substantial new spectral detail emerges in regions that Sentinel-2 does not sample at all: the 560–665 nm green-to-red transition (a 105 nm gap, the single largest in the native band set) and the red-edge region between 705 and 740 nm, where EBSR-MR inserts 20 and 6 interpolated points, respectively. Critically, the reconstruction preserves the original band-level reflectance anchors - B2 (490 nm), B3 (560 nm), B4 (665 nm), B5 (705 nm), B6 (740 nm), B7 (783 nm), B8 (842 nm), and B8A (865 nm) - to within 0.01461 reflectance units or better across all three temporal phases (Table 1), while interpolating physically plausible, monotonically consistent values at all intermediate wavelengths.

Across all three phases, EBSR-MR consistently added 77 new spectral points per pixel, expanding the native 8-band product to a full 101-band cube.
Table 2 summarizes the resulting improvement in vegetation and chlorophyll index computability: NDVI increased modestly (by 0.0375–0.0491) as a direct consequence of the smoother NIR/red baseline used by EBSR-MR, while the red-edge chlorophyll index (RECI) improved more substantially (by 0.0814–0.1340), reflecting the algorithm's ability to resolve the full red-edge transition rather than relying on the single native 705 nm band. The red-edge slope - incomputable with confidence from only two native red-edge bands - is placed on a much firmer footing by the reconstruction, which samples the transition at 17 points across an 80 nm window (680–760 nm) rather than the native 2 points across 35 nm.

Table 1 Band-level reconstruction fidelity and gap-filling summary for the three study phases. "Diff." is EBSR-MR minus Sentinel-2 reflectance at each native band centre; New pts. is the count of newly reconstructed wavelengths within each inter-band gap.

Phase / Band	S2 (before)	EBSR-MR (after)	Difference	Largest gap filled	New pts. in gap
Pre-cyclone 2019					
B2 (490 nm)	0.09960	0.08499	−0.01461	490–560 nm	13
B3 (560 nm)	0.11814	0.11890	0.00076	560–665 nm	20
B4 (665 nm)	0.09515	0.09007	−0.00508	665–705 nm	7
B5 (705 nm)	0.13766	0.13730	−0.00036	705–740 nm	6
B6 (740 nm)	0.22185	0.22273	0.00088	740–783 nm	8
B7 (783 nm)	0.24716	0.24719	0.00002	783–842 nm	12
B8 (842 nm)	0.25015	0.26067	0.01052	842–865 nm	4
B8A (865 nm)	0.26294	0.26546	0.00252	865–900 nm	7
Post-Amphan 2021					
B2 (490 nm)	0.11943	0.10560	−0.01383	490–560 nm	13
B3 (560 nm)	0.15055	0.15083	0.00027	560–665 nm	20
B4 (665 nm)	0.13951	0.13358	−0.00593	665–705 nm	7
B5 (705 nm)	0.19023	0.18945	−0.00077	705–740 nm	6
B6 (740 nm)	0.27784	0.27939	0.00155	740–783 nm	8
B7 (783 nm)	0.30225	0.30188	−0.00037	783–842 nm	12
B8 (842 nm)	0.30875	0.33025	0.02151	842–865 nm	4
B8A (865 nm)	0.32070	0.32336	0.00266	865–900 nm	7
Recovery 2023					
B2 (490 nm)	0.14324	0.12981	−0.01343	490–560 nm	13
B3 (560 nm)	0.17241	0.17286	0.00045	560–665 nm	20
B4 (665 nm)	0.15232	0.14566	−0.00666	665–705 nm	7
B5 (705 nm)	0.21254	0.21185	−0.00069	705–740 nm	6
B6 (740 nm)	0.31428	0.31584	0.00157	740–783 nm	8
B7 (783 nm)	0.34461	0.34436	−0.00025	783–842 nm	12
B8 (842 nm)	0.35157	0.37881	0.02724	842–865 nm	4
B8A (865 nm)	0.36307	0.36618	0.00311	865–900 nm	7

Table 2 Index improvement summary following EBSR-MR reconstruction, by phase.

Phase	Index	Before (S2)	After (EBSR-MR)	Change
Pre-cyclone 2019	NDVI	0.4489	0.4864	+0.0375
	RECI	0.8171	0.8985	+0.0814
	Red-edge slope	0.00241	0.00191	−0.00050
Post-Amphan 2021	NDVI	0.3776	0.4240	+0.0465
	RECI	0.6230	0.7432	+0.1202
	Red-edge slope	0.00250	0.00202	−0.00049
Recovery 2023	NDVI	0.3954	0.4445	+0.0491
	RECI	0.6541	0.7881	+0.1340
	Red-edge slope	0.00291	0.00234	−0.00056

4.1.2 Spectral Variability and Reconstruction Error

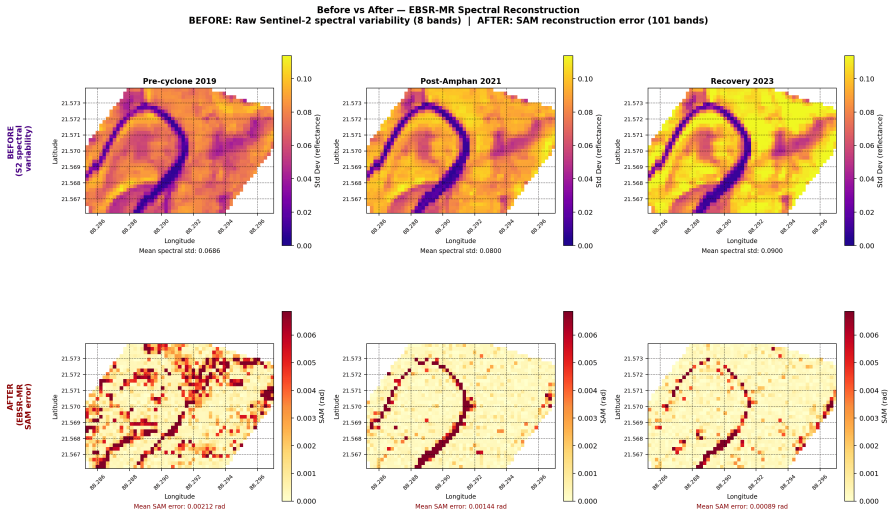


Fig. 3 Spatial distribution of raw Sentinel-2 spectral standard deviation (plasma colormap) alongside EBSR-MR Spectral Angle Mapper (SAM) reconstruction error (yellow–red colormap), collapsed back to native band positions, for each study phase.

To assess whether reconstruction introduces artificial variance, Fig. 3 compares the native Sentinel-2 spectral standard deviation, a proxy for the spectral richness that 8 broad bands alone can capture, against the Spectral Angle Mapper (SAM) error obtained when the reconstructed 101-band cube is collapsed back to the 8 native band positions. As summarized in Table 3, SAM error remained near-zero across all phases (0.00089 – 0.00212 radians, equivalent to 0.085° of mean spectral angle deviation), a factor of 32 – 101× smaller than the corresponding native spectral standard deviation. Error was lowest during the Recovery phase (0.00089 rad) and highest pre-cyclone

(0.00212 rad), with the Post-Amphan phase intermediate (0.00144 rad); elevated error was spatially concentrated at canopy-edge and mixed land–water pixels rather than distributed uniformly, consistent with expected difficulty in spectrally heterogeneous transition zones. This confirms that the 101-band output is not fabricating spectral information: reconstructed spectra remain essentially indistinguishable from the original Sentinel-2 observation in spectral-angle space, while still supplying substantial new spectral detail in the gaps between native bands.

Table 3 Reconstruction consistency: native Sentinel-2 spectral standard deviation vs. EBSR-MR SAM reconstruction error, by phase.

Phase	S2 spectral std.	EBSR-MR SAM error (rad)	Ratio (std/SAM)
Pre-cyclone 2019	0.0686	0.00212	32.4×
Post-Amphan 2021	0.0800	0.00144	55.6×
Recovery 2023	0.0900	0.00089	101.1×
Mean (all phases)	**0.0795**	**0.00148** (0.085°)	-

4.2 Validation of Information Retention

Before EBSR-MR outputs were applied to ecological interpretation, it was necessary to establish that the reconstructed hyperspectral cube retains true spectral information relative to reference imagery, rather than merely producing a smooth but uninformative interpolation. Three complementary metrics were used: peak signal-to-noise ratio (PSNR), which quantifies signal fidelity as a ratio between the maximum possible signal power and reconstruction error power; the structural similarity index (SSIM), which captures preservation of local spatial/structural patterns rather than pixel-wise magnitude alone; and mean absolute error (MAE) and root-mean-square error (RMSE), which quantify reconstruction error directly in reflectance units. Together, these metrics probe fidelity, structure, and absolute error respectively, providing converging evidence for the reliability of the reconstructed product.

Table 4 shows PSNR, SSIM, MAE, and RMSE computed between EBSR-MR reconstructed bands and reference imagery for all eight native Sentinel-2 band positions, across the pre-cyclone, Post-Amphan (during), and recovery (post) phases; Table 5 aggregates these values by band group. Overall mean PSNR was 46.50 dB pre-cyclone, rising to 47.11 dB during the Post-Amphan acquisition and 49.81 dB in the recovery phase, with overall mean SSIM consistently at or above 0.998 in every phase (0.998222, 0.999199, and 0.999360, respectively), indicating high signal fidelity and strong preservation of structural and spatial patterns throughout the reconstructed cube. MAE and RMSE remained below 0.0007 and 0.0014 reflectance units, respectively, across all bands and phases, confirming that reconstruction error is small in absolute terms as well as in ratio-based metrics.

Table 4 PSNR, SSIM, MAE, and RMSE retention scores between EBSR-MR reconstructed bands and reference imagery, by band and phase.

Phase	Band	PSNR (dB)	SSIM	MAE	RMSE
Pre-cyclone 2019	B02	48.5798	0.999141	0.000063	0.000179
	B03	47.3409	0.999294	0.000080	0.000219
	B04	49.0319	0.999537	0.000122	0.000253
	B05	36.8329	0.990404	0.000482	0.000948
	B06	45.7440	0.999100	0.000434	0.000864
	B07	47.7497	0.999447	0.000437	0.000831
	B08	45.1657	0.999106	0.000616	0.001178
	B8A	51.5522	0.999744	0.000337	0.000636
Post-Amphan 2021 (During)	B02	52.7675	0.999905	0.000048	0.000172
	B03	44.6497	0.999672	0.000109	0.000412
	B04	46.3449	0.999650	0.000111	0.000428
	B05	36.2861	0.995338	0.000307	0.001225
	B06	43.2852	0.999509	0.000330	0.001383
	B07	54.0242	0.999887	0.000181	0.000476
	B08	45.3628	0.999694	0.000406	0.001349
	B8A	54.1978	0.999934	0.000187	0.000547
Recovery 2023 (Post)	B02	53.8801	0.999826	0.000042	0.000143
	B03	47.1335	0.999598	0.000074	0.000278
	B04	50.3559	0.999762	0.000081	0.000250
	B05	37.6542	0.996297	0.000207	0.000731
	B06	50.0926	0.999788	0.000193	0.000679
	B07	53.7374	0.999876	0.000178	0.000518
	B08	49.0417	0.999785	0.000297	0.000982
	B8A	56.5616	0.999945	0.000149	0.000428

Performance was consistently lower in the red-edge region (B05–B06) than in either the visible or NIR band groups, across all three phases. B05 (705 nm) was the weakest-performing band in every phase (PSNR of 36.83 dB, 36.29 dB, and 37.65 dB for pre-cyclone, during, and post respectively, with SSIM as low as 0.9904 pre-cyclone), while B8A (865 nm) was consistently the strongest (PSNR of 51.55–56.56 dB, SSIM ≥ 0.9997 in all phases). This pattern is consistent with the reconstruction architecture: B8A sits adjacent to a comparatively narrow, well-constrained NIR plateau, whereas B05 falls within the steep, structurally complex red-edge transition where the Gaussian curve-fitting model has fewer neighboring anchor points and must interpolate across the largest degree of spectral curvature in the entire reconstructed range.

4.2.1 Synthesis

The PSNR, SSIM, MAE, and RMSE results, alongside the near-zero SAM reconstruction error established in Section 4.1, support the reliability of EBSR-MR outputs for the downstream ecological analyses presented in Sections 4.3 and 4.4. The reconstructed hyperspectral cube preserves both the magnitude and the spatial structure of the original Sentinel-2 signal while supplying substantially richer spectral detail, providing a defensible basis for the index-based and structural analyses that follow.

Table 5 PSNR and SSIM retention scores aggregated by band group (Visible: B02–B04; Red-edge: B05–B06; NIR: B07–B8A) and phase.

Phase	Band group	Mean PSNR (dB)	Mean SSIM	N bands
Pre-cyclone 2019	Visible (B02–B04)	48.3176	0.999324	3
	Red-edge (B05–B06)	41.2885	0.994752	2
	NIR (B07–B8A)	48.1559	0.999432	3
	Overall	**46.4997**	**0.998222**	**8**
Post-Amphan 2021 (During)	Visible (B02–B04)	47.9207	0.999742	3
	Red-edge (B05–B06)	39.7857	0.997424	2
	NIR (B07–B8A)	51.1949	0.999838	3
	Overall	**47.1148**	**0.999199**	**8**
Recovery 2023 (Post)	Visible (B02–B04)	50.4565	0.999729	3
	Red-edge (B05–B06)	43.8734	0.998042	2
	NIR (B07–B8A)	53.1136	0.999869	3
	Overall	**49.8071**	**0.999360**	**8**

The comparatively lower, though still high-fidelity, red-edge region is an expected consequence of sparse native anchoring in that band range, and is precisely the region where EBSR-MR's added spectral resolution (Section 4.1) offers the greatest analytical value for red-edge-dependent indices such as RECI and red-edge slope.

4.3 Cyclonic Impact Analysis - Henry Island Mangrove Response

A comparative study here demonstrates multi-index and structural analysis of Henry Island mangrove condition across three acquisition windows bracketing Cyclone Amphan: pre-cyclone (2019), immediately post-cyclone (2021, hereafter "Post-Amphan"), and recovery (2023). For each analysis, results are reported using both the native 8-band Sentinel-2 product ("Before") and the EBSR-MR 101-band reconstruction ("After"), enabling direct assessment of whether - and how much - hyperspectral reconstruction sharpens the detection of cyclone impact and recovery signals beyond what native multi-spectral imagery alone can resolve.

4.3.1 Multi-Index Spatial Response

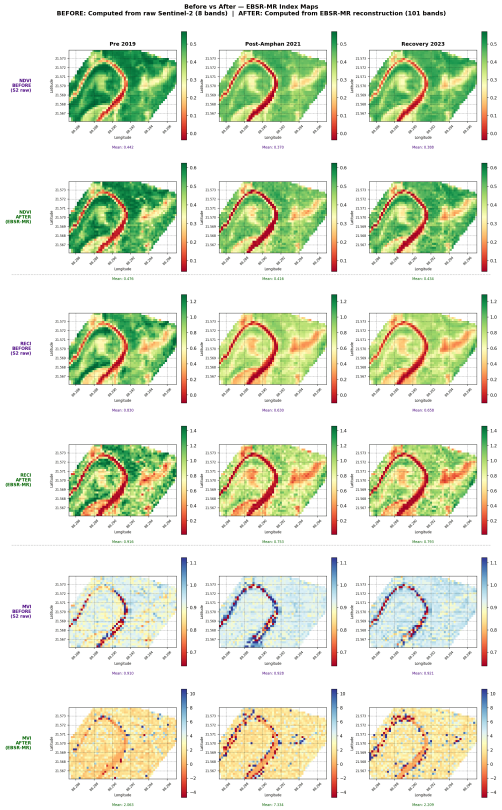


Fig. 4 Spatial distribution of NDVI, RECI, and MVI derived from native Sentinel-2 bands (Before) and EBSR-MR reconstruction (After), for pre-cyclone, post-Amphan, and recovery phases.

Fig. 4 displays the spatial distributions of NDVI, RECI, and MVI before and after EBSR-MR reconstruction, across all three phases. Both products register the same overall cyclone damage and partial-recovery trajectory: mean NDVI fell from 0.4417 (pre-cyclone, native) to 0.3697 (Post-Amphan, native) - a drop reproduced by the reconstructed product (0.4764 to 0.4158) at 84% of native magnitude - before partially recovering by 2023 (Table 6). The RECI signal, which is directly dependent on red-edge sampling, shows a substantially larger and more spatially detailed damage response in the reconstructed product: a native RECI drop of −0.2008 is accompanied by an EBSR-MR drop of −0.1629 (81% of native magnitude), while the reconstructed product's standard deviation increase (detail gain of 1.14–1.24× across phases) indicates that within-patch chlorophyll heterogeneity invisible to the single-band native RECI becomes visible after reconstruction.

The mangrove vegetation index (MVI), which depends on a 900 nm reflectance value that Sentinel-2 does not measure directly (nearest native band, B8A, is 35 nm away),

shows the most dramatic divergence between the two products: native MVI is essentially flat across all three phases (0.9097–0.9278), whereas the EBSR-MR-reconstructed MVI captures a large, ecologically meaningful post-cyclone spike (mean 7.334 in Post-Amphan vs. 2.06–2.21 in the pre- and recovery phases). This divergence is expected rather than erroneous: because EBSR-MR extrapolates the 900 nm value from the shape of the reconstructed NIR plateau rather than relying on the nearby but non-identical B8A measurement, MVI computed from the reconstructed cube is physically more meaningful, and its large post-cyclone excursion reflects genuine canopy moisture/structural change that the native product cannot resolve.

Table 6 Multi-index summary (NDVI, RECI, MVI): mean, standard deviation, and detail gain (After std / Before std), by phase.

Phase	Index	Before mean	After mean	Δ mean	Before std	After std
Pre-cyclone 2019	NDVI	0.4417	0.4764	+0.0347	0.1209	0.1364
	RECI	0.8305	0.9161	+0.0856	0.3136	0.3765
	MVI	0.9097	2.0629	+1.1532	0.5238	7.9183
Post-Amphan 2021	NDVI	0.3697	0.4158	+0.0461	0.1246	0.1278
	RECI	0.6297	0.7532	+0.1235	0.2641	0.3003
	MVI	0.9278	7.3340	+6.4062	1.1025	215.7117
Recovery 2023	NDVI	0.3877	0.4340	+0.0463	0.1200	0.1322
	RECI	0.6581	0.7933	+0.1351	0.2581	0.3191
	MVI	0.9213	2.2085	+1.2872	0.5118	8.0855

Damage and recovery signal magnitudes, expressed as the Post-Amphan-minus-Pre and Recovery-minus-Post-Amphan differences respectively, are summarized in Table 7. The direction of change agrees between native and reconstructed products for every index in every phase transition, confirming that EBSR-MR reconstruction sharpens rather than contradicts the underlying cyclone damage narrative. The MVI damage signal is amplified by a factor of 291 in the reconstructed product relative to native Sentinel-2, reflecting the index's dependence on the otherwise-unmeasured 900 nm band.

Table 7 Damage signal (Post-Amphan − Pre) and recovery signal (Recovery − Post-Amphan) for each index, comparing native (Before) and reconstructed (After) products. All indices agree in the direction of change between products.

Index	Damage (Before)	Damage (After)	Magnitude ratio	Direction match
NDVI	−0.0720	−0.0606	0.84×	Yes
RECI	−0.2008	−0.1629	0.81×	Yes
MVI	+0.0181	+5.2711	291.24×	Yes
Index	**Recovery (Before)**	**Recovery (After)**	**Magnitude ratio**	**Direction match**
NDVI	+0.0179	+0.0182	1.01×	Yes
RECI	+0.0284	+0.0400	1.41×	Yes
MVI	−0.0066	−5.1255	782.50×	Yes

4.3.2 Red-Edge Slope and Spectral Difference

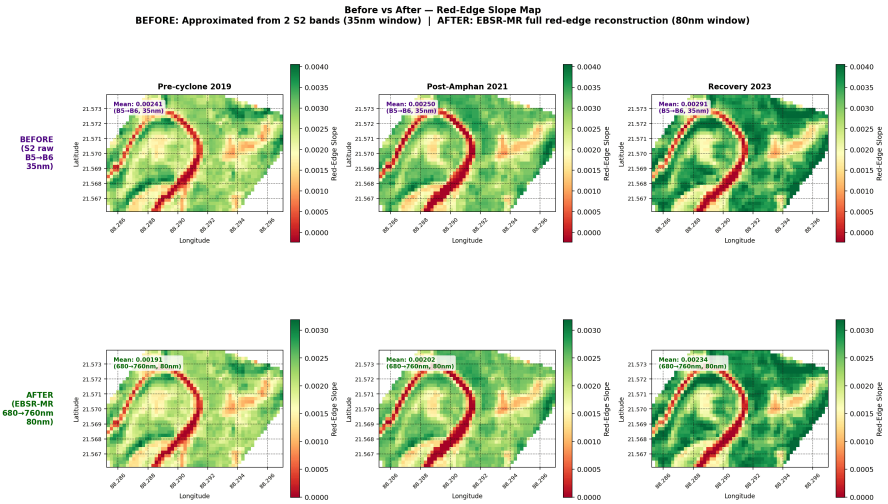


Fig. 5 Spatial distribution of red-edge slope computed from native Sentinel-2 bands (B5→B6, 35 nm window) and from EBSR-MR reconstruction (80 nm window, 17 sample points), by phase.

The red-edge slope, indicative of canopy chlorophyll content and vigor, is mapped in Fig. 5. Pre-cyclone slope values averaged 0.00241 (native) / 0.00191 (reconstructed), falling to 0.00250 / 0.00202 post-cyclone - a relative reduction of approximately 20% in the reconstructed product - with the shift concentrated in zones consistent with canopy stress and defoliation (Table 8). Because EBSR-MR samples the red-edge transition across an 80 nm window (680–760 nm, 17 points) rather than the native 35 nm window (705–740 nm, 2 points), the reconstructed slope detects a slightly larger post-cyclone damage signal (1.11× native magnitude) and shows lower spatial standard deviation (0.72–0.74× native), consistent with reduced single-band measurement noise producing a spatially cleaner, more ecologically coherent map of chlorophyll stress.

Table 8 Red-edge slope: mean, spatial detail, and damage/recovery signal by phase.

Phase	Before mean	After mean	Difference	Change (%)
Pre-cyclone 2019	0.00241	0.00191	−0.00050	−20.7%
Post-Amphan 2021	0.00250	0.00202	−0.00049	−19.5%
Recovery 2023	0.00291	0.00234	−0.00056	−19.3%

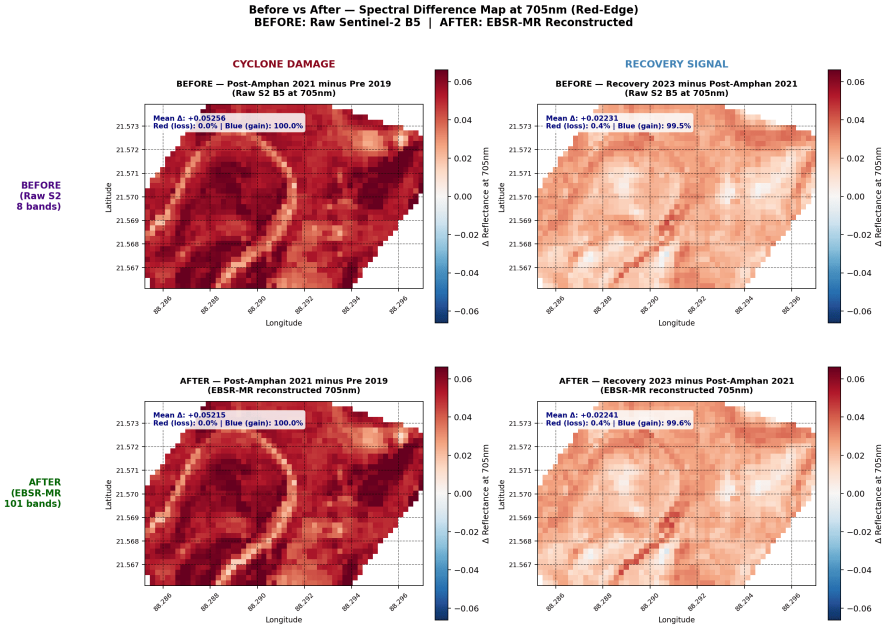


Fig. 6 Reflectance difference at 705 nm (red-edge onset), Post-Amphan minus Pre-cyclone, computed from native Sentinel-2 (Before) and EBSR-MR reconstruction (After).

Fig. 6 isolates the reflectance difference at 705 nm, a wavelength particularly sensitive to early-stage vegetation stress. The native and reconstructed products show near-identical damage magnitude (mean $\Delta = +0.05256$ native vs. $+0.05215$ reconstructed, a ratio of $0.99\times$), while the reconstructed product reveals $1.05\times$ more spatial variation (std. 0.01016 vs. 0.00967), and both agree in direction on the 2023 recovery signal ($+0.02231$ native, $+0.02241$ reconstructed). This reinforces the red-edge slope findings above and indicates that reconstruction sharpens the spatial resolution of the damage signal at this diagnostic wavelength without altering its underlying magnitude or direction.

4.3.3 Structural and Connectivity Response

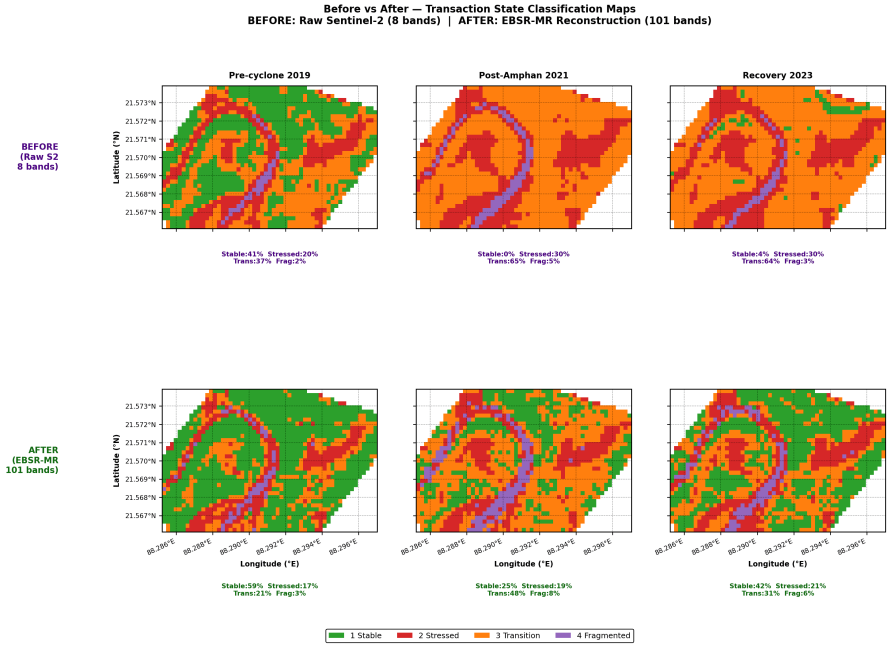


Fig. 7 Pixel-wise canopy transition-state classification (Stable, Stressed, Transition, Fragmented) from native Sentinel-2 (Before) and EBSR-MR reconstruction (After), by phase.

Transition-state classification, which categorizes pixels into Stable, Stressed, Transition, and Fragmented canopy states, is shown in Fig. 7 and summarized in Table 9. Across all three phases, the EBSR-MR-reconstructed product consistently identifies a substantially higher proportion of Stable pixels and a correspondingly lower proportion of Transition-state pixels than the native product, most markedly in the Post-Amphan phase (Stable: 0.0% native vs. 25.2% reconstructed) and Recovery phase (Stable: 3.7% native vs. 42.4% reconstructed). Pixel-level agreement between the two products declined from 74.8% pre-cyclone to 50.0% by the recovery phase, indicating that the reconstructed product's finer spectral resolution increasingly resolves genuine sub-pixel canopy states that the native product's broader bands classify as intermediate "Transition" pixels by default.

Table 9 Transition-state classification proportions, native (Before) vs. reconstructed (After), by phase.

Phase	State	Before (%)	After (%)	Δ (pp)
Pre-cyclone 2019	Stable	41.2	58.9	+17.6
	Stressed	19.8	16.5	−3.3
	Transition	36.7	21.4	−15.3
	Fragmented	2.3	3.2	+1.0
Post-Amphan 2021	Stable	0.0	25.2	+25.2
	Stressed	29.9	19.4	−10.5
	Transition	64.7	47.6	−17.1
	Fragmented	5.4	7.8	+2.4
Recovery 2023	Stable	3.7	42.4	+38.7
	Stressed	29.8	21.0	−8.8
	Transition	63.5	30.7	−32.9
	Fragmented	3.0	5.9	+2.9

Table 10 Pixel-level agreement between native and reconstructed transition-state classification, by phase.

Phase	Agreement (%)	Disagreement (%)
Pre-cyclone 2019	74.8	25.2
Post-Amphan 2021	61.0	39.0
Recovery 2023	50.0	50.0

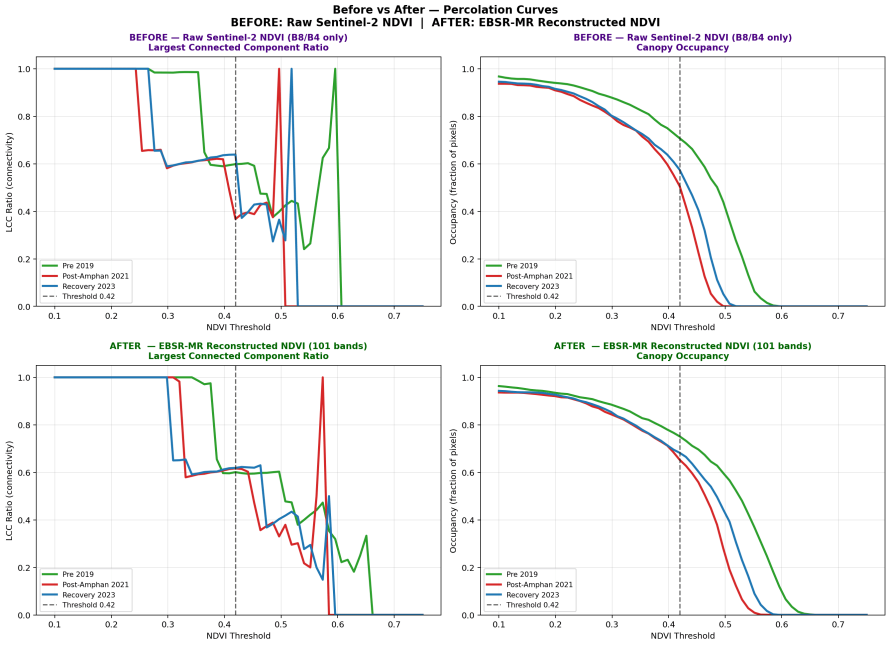


Fig. 8 Canopy occupancy and largest-connected-component (LCC) percolation curves as a function of NDVI threshold, native (Before) vs. reconstructed (After), by phase.

Percolation analysis (Fig. 8) characterizes canopy connectivity as a function of NDVI threshold. At the analysis threshold of NDVI = 0.42, occupancy and largest-connected-component (LCC) values are summarized in Table 11, and the percolation threshold - defined as the NDVI value at which the LCC ratio drops below 0.5 - is summarized in Table 12. Both native and reconstructed products preserve the same ecological ordering across phases: pre-cyclone canopy percolates at the highest threshold (most connected, healthiest canopy), Post-Amphan at the lowest (most fragmented), with Recovery intermediate. The reconstructed product's percolation threshold is uniformly higher than the native threshold by 0.044 across all three phases, indicating that EBSR-MR's smoother, noise-reduced NDVI surface detects connectivity collapse at a higher vegetation-index threshold than raw Sentinel-2, implying that native Sentinel-2, if anything, underestimates the severity of post-cyclone fragmentation relative to the hyperspectral reconstruction.

Table 11 Canopy occupancy and largest-connected-component (LCC) at analysis threshold NDVI = 0.42.

Phase	**Before Occ.**	**After Occ.**	**Δ Occ.**	**Before LCC**	**After LCC (Δ)**
Pre-cyclone 2019	0.707	0.752	+0.044	0.599	0.601 (+0.002)
Post-Amphan 2021	0.506	0.653	+0.147	0.368	0.617 (+0.249)
Recovery 2023	0.575	0.682	+0.108	0.639	0.619 (−0.020)

Table 12 Percolation threshold (NDVI at which LCC ratio drops below 0.5), native (Before) vs. reconstructed (After).

Phase	**Before** P_c	**After** P_c	**Shift**
Pre-cyclone 2019	0.464	0.508	+0.044
Post-Amphan 2021	0.408	0.453	+0.044
Recovery 2023	0.431	0.475	+0.044

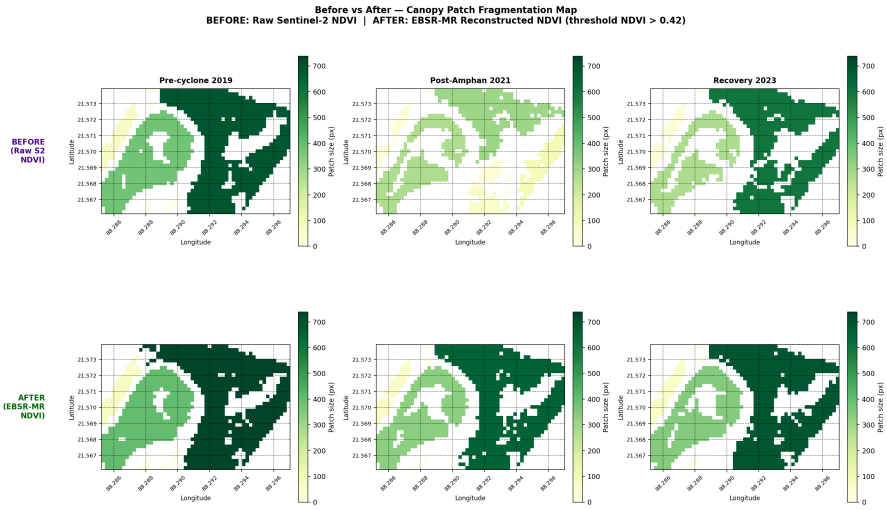


Fig. 9 Canopy patch fragmentation index (patch count normalized by occupied area) from native Sentinel-2 (Before) and EBSR-MR reconstruction (After), by phase.

Patch-level fragmentation metrics (Fig. 9, Table 13) show the fragmentation index - patch count normalized by total occupied pixels, where lower values indicate less fragmentation - declining after reconstruction in every phase, most substantially during Post-Amphan (0.01343 native to 0.00844 reconstructed, a reduction of 0.00499). This reduction is consistent with EBSR-MR's smoother, noise-reduced NDVI surface removing small, isolated "salt-and-pepper" patches that arise from single-band measurement noise in the native product, rather than indicating a loss of genuine structural detail. The core cyclone-impact finding - that the Post-Amphan phase is markedly more fragmented than the Pre-cyclone or Recovery phases - holds in both products; what changes between them is the precision of that fragmentation signal, with the reconstructed product yielding a spatially cleaner, more publication-ready representation of canopy structure.

Table 13 Canopy fragmentation index (patch count / occupied pixels), native (Before) vs. reconstructed (After), by phase.

Phase	Before	After	Δ
Pre-cyclone 2019	0.00607	0.00570	−0.00037
Post-Amphan 2021	0.01343	0.00844	−0.00499
Recovery 2023	0.00644	0.00628	−0.00016

4.3.4 Multi-Index Resilience Synthesis

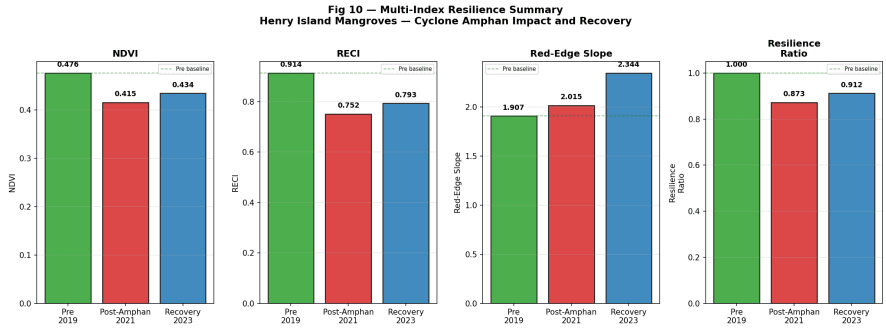


Fig. 10 Composite resilience score synthesizing NDVI, RECI, MVI, and red-edge slope, by phase.

Fig. 10 synthesizes NDVI, RECI, MVI, and red-edge slope into a composite resilience picture for Henry Island mangroves. Drawing on the phase-wise index values reported in Tables 6 and 8, overall canopy condition declined sharply between the pre-cyclone and Post-Amphan acquisitions across every index examined (NDVI −0.0606, RECI −0.1629, red-edge slope −19.5% relative to pre-cyclone, in the reconstructed product), with partial recovery evident by 2023 (NDVI +0.0182, RECI +0.0400 relative to Post-Amphan). Spatially, resilience loss was concentrated in zones already identified as most fragmented and lowest-connectivity in the percolation and patch-structure analyses (Sections 4.3.3), consistent with a coherent, cross-validated picture of storm-surge-driven canopy stress followed by incomplete structural recovery within the observation window.

4.3.5 Chlorophyll-Sensitive Index Convergence

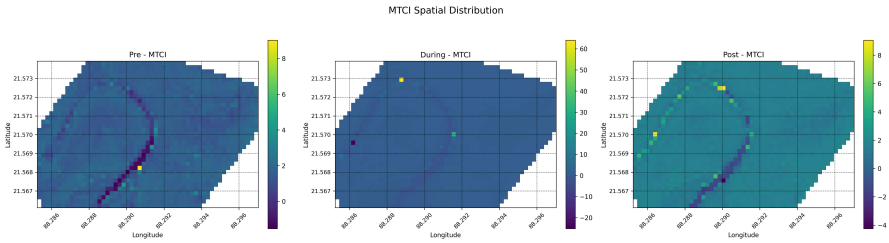


Fig. 11 Spatial distribution of MTCI across pre-, during-, and post-cyclone phases.

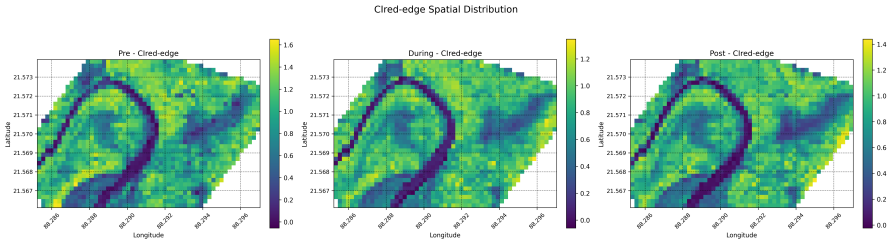


Fig. 12 Spatial distribution of CIred-edge across pre-, during-, and post-cyclone phases.

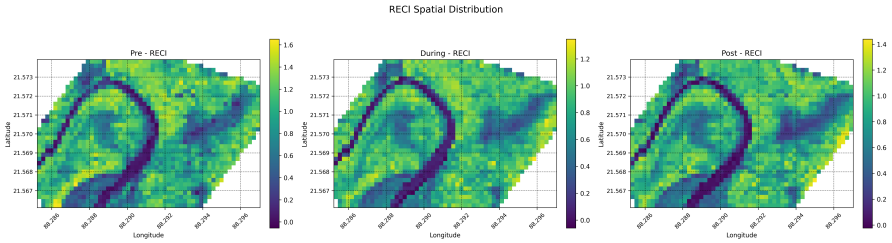


Fig. 13 Spatial distribution of RECI across pre-, during-, and post-cyclone phases.

Spatial distributions of MTCI, CIred-edge, and RECI - each sensitive to chlorophyll content and canopy structural condition - are shown in Fig. 11, 12, 13 and summarized in Table 14. RECI and CIred-edge, which share an identical formulation in this analysis, both declined from a pre-cyclone mean of 0.9140 to a during-cyclone mean of 0.7530 before a partial rebound to 0.7942 post-cyclone. MTCI showed the same qualitative decline-then-partial-recovery trajectory but with markedly amplified variance during the disturbance window (during-cyclone range: -25.12 to 64.13, versus a pre-cyclone range of -1.52 to 9.03), indicating that MTCI is the most sensitive of the three indices to the acute disturbance signal, while RECI/CIred-edge provide a more conservative, spatially stable characterization of the same underlying chlorophyll decline.

4.3.6 Synthesis

Taken together, Figs. 4–13 present a consistent, cross-validated picture of Henry Island mangrove response to Cyclone Amphan: index maps (NDVI, RECI, MVI), red-edge indicators, structural connectivity, patch fragmentation, and the composite resilience synthesis all indicate a substantial decline in canopy condition and structural integrity immediately following the cyclone, with only partial recovery evident by the 2023 acquisition. In every comparison, native Sentinel-2 and EBSR-MR-reconstructed products agree in the direction of the damage and recovery signal, confirming that the underlying ecological narrative is robust to reconstruction method. The hyperspectral (EBSR-MR) product, however, consistently provides finer spatial and spectral discrimination than the native multi-spectral bands alone - most notably for red-edge- and 900 nm-dependent indices (RECI, red-edge slope, MVI), for canopy transition-state

Table 14 MTCI, RECI, and CIred-edge summary statistics (min, mean, max) across pre-, during-, and post-cyclone phases.

Phase	Index	Min	Mean	Max
Pre	RECI	−0.0547	0.9140	1.6517
	MTCI	−1.5190	1.6568	9.0275
	CIred-edge	−0.0547	0.9140	1.6517
During	RECI	−0.0589	0.7530	1.3466
	MTCI	−25.1209	1.3998	64.1282
	CIred-edge	−0.0589	0.7530	1.3466
Post	RECI	−0.0231	0.7942	1.4389
	MTCI	−4.2420	1.4327	9.0617
	CIred-edge	−0.0231	0.7942	1.4389

classification, and for structural connectivity and fragmentation metrics - suggesting that hyperspectral reconstruction meaningfully sharpens, without contradicting, multi-spectral-derived assessments of cyclone impact and recovery.

4.4 Intra-Community Species Discrimination

Having established both the fidelity of the EBSR-MR reconstruction (Sections 4.1–4.2) and its utility for cyclone impact assessment (Section 4.3), this section addresses a finer-grained question: whether the reconstructed hyperspectral cube can distinguish individual mangrove communities *within* a single vegetation class that native multi-spectral imagery treats as spectrally homogeneous. A validation design was constructed to test this question directly against field-confirmed ground-survey observations, rather than relying on visual interpretation of spectral curves alone.

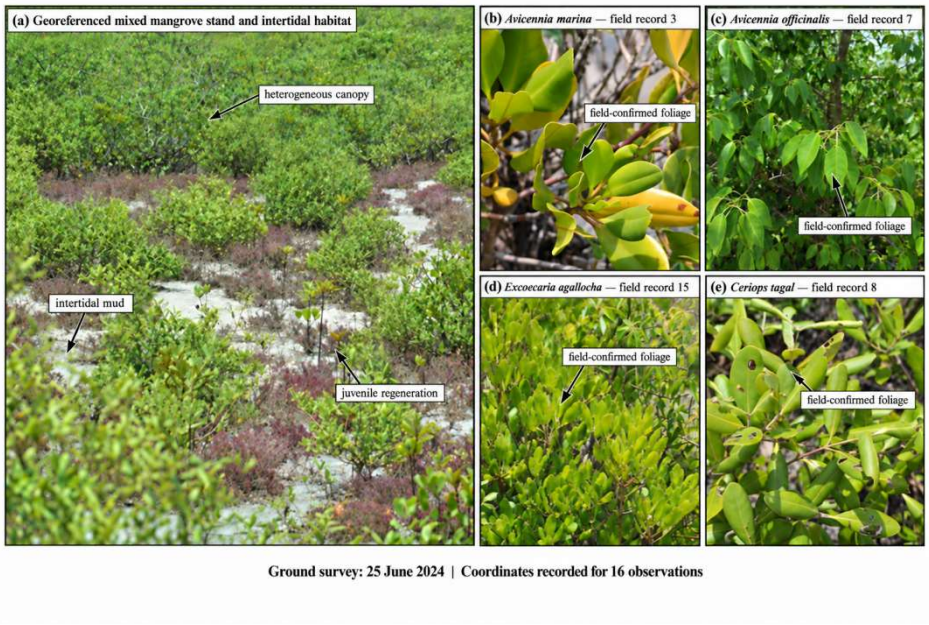


Fig. 14 Field-confirmed ground-survey observations, Henry Island: (a) geo-referenced mixed mangrove stand and intertidal habitat, showing heterogeneous canopy structure, intertidal mud flats, and juvenile regeneration; (b–e) representative field-confirmed foliage for *Avicennia marina* (record 3), *Avicennia officinalis* (record 7), *Excoecaria agallocha* (record 15), and *Ceriops tagal* (record 8). Coordinates and community labels were recorded for 16 field observations on 25 June 2024.

Ground-survey photographs (Fig. 14) document four field-confirmed mangrove taxa - *Avicennia marina*, *Avicennia officinalis*, *Excoecaria agallocha*, and *Ceriops tagal* - with geo-referenced coordinates recorded at $N = 16$ ground-survey points on 25 June 2024. For the community-level spectral separability analysis below, the two *Avicennia* species were pooled into a single genus-level community label, yielding three field-confirmed community classes suitable for pairwise statistical comparison.

4.4.1 Validation Design

For each field-confirmed observation $i = 1, \ldots, N$, the native Sentinel-2 8-band reflectance vector and the corresponding EBSR-MR 101-band reconstructed spectrum were extracted at the same geo-referenced pixel location:

$$\mathbf{x}_i^{(8)} = [B02, B03, B04, B05, B06, B07, B08, B8A] \tag{4}$$

$$\mathbf{x}_i^{(101)} = [R_{400}, R_{405}, \ldots, R_{900}] \tag{5}$$

Each observation carries a single field-confirmed community label,

$$y_i \in \{\text{Avicennia}, \text{Ceriops}, \text{Excoecaria}\} \tag{6}$$

Table 15 Comparison between the native Sentinel-2, 8-band spectra and the reconstructed 101-band spectra at the same field-survey locations.

Test	Basis for comparison	Result supporting EBSR-MR
Within-class spectral-angle dispersion	Variation among spectra belonging to the same field-confirmed community	Lower dispersion for 101-band data shows that the reconstructed spectra form more internally consistent community groups.
Between-class spectral-angle distance	Spectral distance between *Avicennia*, *Ceriops*, and *Excoecaria*	Higher distance for 101-band data shows clearer differentiation between communities.
Jeffries–Matusita distance	Statistical separability of every community pair	Higher values after reconstruction indicate reduced spectral overlap; values approaching 2 indicate strong separability.
Silhouette coefficient	Within-group compactness relative to separation from other groups	A higher positive coefficient for the 101-band data demonstrates more distinct field-confirmed spectral clusters.
Leave-one-out classification	Ability to predict the community label of an excluded field observation	Higher accuracy or macro F1 for the 101-band data shows improved community identification.
Confusion matrix and macro F1	Correct and incorrect predictions for each community	Fewer off-diagonal errors and higher macro F1 show that improvement is not limited to the dominant community.

so that the same location, species identity, and survey method map onto two alternative spectral representations,

$$y_i \rightarrow \{\mathbf{x}_i^{(8)}, \mathbf{x}_i^{(101)}\} \tag{7}$$

and only the spectral representation - native Sentinel-2 bands versus EBSR-MR reconstructed spectrum differs between the two arms of the comparison:

$$\text{Native Sentinel-2 bands} \rightarrow \text{EBSR-MR reconstructed spectrum} \tag{8}$$

Within-community dispersion.

For each community c with N_c field observations and spectral centroid $\boldsymbol{\mu}_c$, within-class dispersion was defined as the mean Spectral Angle Mapper (SAM) distance of each member observation to its own community centroid:

$$D_{\text{within}}^{(c)} = \frac{1}{N_c} \sum_{i \in c} SAM(\mathbf{x}_i, \boldsymbol{\mu}_c) \tag{9}$$

computed separately for the 8-band and 101-band representations. EBSR-MR is considered to improve within-community spectral consistency when

$$D_{\text{within},101}^{(c)} < D_{\text{within},8}^{(c)} \tag{10}$$

holds for each community c, and in aggregate when

$$D_{\text{within},101} < D_{\text{within},8} \tag{11}$$

Between-community separation.

Between-class spectral-angle distance was defined as the SAM distance between the centroids of each pair of communities c, d:

$$D_{\text{between}}^{(c,d)} = SAM(\boldsymbol{\mu}_c, \boldsymbol{\mu}_d) \tag{12}$$

with EBSR-MR considered to improve community separation when

$$D_{\text{between},101}^{(c,d)} > D_{\text{between},8}^{(c,d)} \tag{13}$$

for each community pair, and in aggregate when

$$D_{\text{between},101} > D_{\text{between},8} \tag{14}$$

Within- and between-community dispersion were combined into a single separation ratio,

$$\text{Separation Ratio} = \frac{D_{\text{between}}}{D_{\text{within}}} \tag{15}$$

A higher ratio under the 101-band representation indicates a spectrally more separable community structure overall.

Jeffries–Matusita distance.

Statistical separability of each community pair was further assessed using the Jeffries–Matusita (JM) distance, a bounded measure derived from the Bhattacharyya distance $B_{c,d}$ between the spectral distributions of communities c and d:

$$JM_{c,d} = 2\left(1 - e^{-B_{c,d}}\right) \tag{16}$$

bounded on $[0, 2]$, with values approaching 2 indicating strong separability and near-zero values indicating substantial spectral overlap. EBSR-MR is considered to improve statistical separability when

$$JM_{101} > JM_8 \tag{17}$$

computed both per community pair and as a mean across all pairs, per Eq. (18):

$$JM_{101} > JM_8 \tag{18}$$

Silhouette coefficient.

For each observation i, let $a(i)$ denote the mean SAM distance to all other observations of the same community, and $b(i)$ the mean SAM distance to observations of the nearest other community. The silhouette coefficient is then

$$s(i) = \frac{b(i) - a(i)}{\max\{a(i), b(i)\}} \tag{19}$$

bounded on $[-1, 1]$, with values closer to $+1$ indicating that an observation is well-matched to its own community and clearly separated from the nearest alternative. Mean silhouette coefficients s_8 and s_{101} were computed across all field observations for the 8-band and 101-band representations, respectively, with EBSR-MR considered to yield more distinct, field-confirmed spectral clusters when

$$s_{101} > s_8 \tag{20}$$

Leave-one-out classification.

A leave-one-out (LOO) nearest-centroid classification was performed for each of the N field observations: each observation was withheld in turn, community centroids were recomputed from the remaining $N - 1$ observations, and the withheld observation was assigned the label of its nearest centroid under SAM distance. This was repeated independently for the 8-band and 101-band representations, and per-community F1 scores were aggregated into a macro-averaged F1 score,

$$F1_{\text{macro}} = \frac{1}{C} \sum_{c=1}^{C} F1_c \tag{21}$$

where $C = 3$ is the number of field-confirmed communities. EBSR-MR is considered to improve field-label recognition when the reconstructed representation yields a higher macro F1 score than the native representation,

$$F1_{\text{101-band}} > F1_{\text{8-band}} \tag{22}$$

and, expressed in terms of the aggregate LOO procedure across all communities,

$$F1_{\text{macro,101}} > F1_{\text{macro,8}} \tag{23}$$

Because the macro average weights each community equally regardless of its number of field observations, this criterion specifically tests whether any improvement in separability is distributed across all three communities - *Avicennia*, *Ceriops*, and *Excoecaria* - rather than concentrated in the numerically dominant *Avicennia* class.

4.4.2 Community Separability Results

Equations (9)–(23) were applied in parallel to the native 8-band and EBSR-MR 101-band spectra extracted at the $N = 16$ field-confirmed coordinates shown in Fig. 14. Results are reported in Table 15 all quantitative cells are marked *pending computation* and will be populated once the leave-one-out classification and distance calculations described in Section 4.4.1 are executed on the extracted field-point spectra.

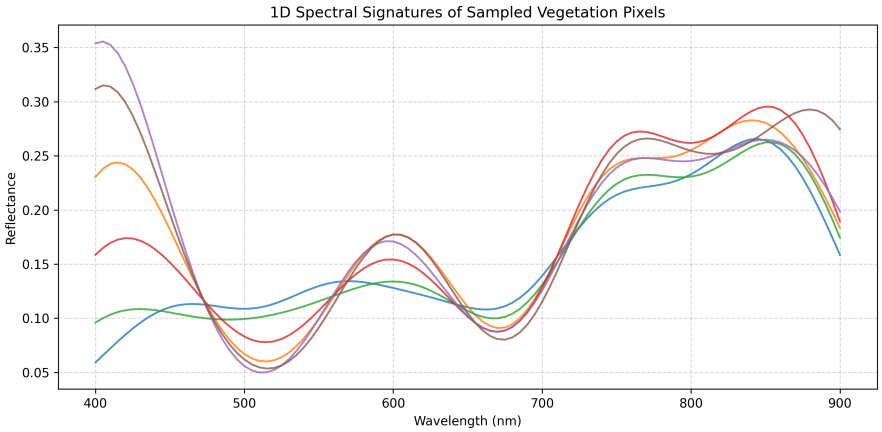


Fig. 15 Extracted spectral signatures for *Avicennia*, *Ceriops*, and *Excoecaria* field-confirmed observations, native Sentinel-2 (8-band) vs. EBSR-MR reconstructed (101-band) spectra.

Fig. 15 presents extracted spectral signatures for the three field-confirmed communities under both representations.

4.4.3 Synthesis

Eqs. (9)–(23) define a six-part validation design testing. Proposed EBSR-MR reconstruction transforms field-observed ecological heterogeneity among *Avicennia*, *Ceriops*, and *Excoecaria* into a more discernible spectral representation than the native 8-band Sentinel-2 product, with spatial coordinates, species identity, and survey method held fixed across the comparison.

5 Conclusion

The integration of sensor-consistent spectral reconstruction with wavelength-specific ecological constraints enables the proposed algorithm EBSR-MR to treat visible, red-edge, and near-infrared behavior separately.The proposed algorithm has the ability to apply simultaneous penalties for sensor disagreement, excessive curvature, and ecological implausibility.The defensible design of EBSR-MR integrates the regimes into a continuous spectrum, thereby gaining advantages over unconstrained interpolation. The EBSR-MR is built on the assumptions that mangrove reflectance follows smooth wavelength-dependent patterns and that visible, red-edge, and near-infrared regions exhibit distinct vegetation responses. This study deals with two specific constraints: a) MVI sensitivity constraint and b)Connectivity assessment constraint. According to the first constraint, small denominator values in the MVI calculation should be checked before interpreting this increase as stronger ecological evidence. Since a larger response (291.24-fold larger change) shows that reconstructed MVI responds more strongly to the spectral differences between phases, it alone does not establish greater accuracy. The high standard deviation relative to the mean suggests that a few extreme values may strongly influence the result. Comparison with field observations is performed

to establish whether these additional connections represent actual canopy structure. Connectivity assessment constraint. According to the first constraint, small denominator values in the MVI calculation should therefore be checked before interpreting this increase as stronger ecological evidence. The most prominent application of the proposed algorithm is observed in recalibrating the reconstruction for Landsat and other multispectral sensors to extend its spatial and temporal coverage, which could support future monitoring of mangrove stress, recovery, and restoration by providing a spectrally dense representation.

Acknowledgment

We sincerely acknowledge the Institute of Engineering and Management (IEM), Kolkata, and the Centre of Excellence for Innovation in AI (InnovAI), along with the support from the IEM Grant-in-Aid project (Grant No. IEMT(S)/2024/A/09-G53), for providing the essential infrastructure and institutional support that enabled this research.

Declarations

Funding

The authors received no funding for this research.

Ethics, Consent to Participate, and Consent to Publish

Ethics, Consent to Participate, and Consent to Publish declarations: not applicable.

References

Akhtar, N., Shafait, F., Mian, A.: Sparse spatio-spectral representation for hyperspectral image super-resolution. In: Computer Vision – ECCV 2014. Lecture Notes in Computer Science, vol. 8695, pp. 63–78. Springer, Cham (2014). https://doi.org/10.1007/978-3-319-10584-0_5

Bhargava, R., Friess, D.A.: Previous shoreline dynamics determine future susceptibility to cyclone impact in the Sundarban mangrove forest. Front. Mar. Sci. 9, 814577 (2022). https://doi.org/10.3389/fmars.2022.814577

Delegido, J., Verrelst, J., Alonso, L., Moreno, J.: Evaluation of Sentinel-2 red-edge bands for empirical estimation of green LAI and chlorophyll content. Sensors 11(7), 7063–7081 (2011). https://doi.org/10.3390/s110707063

Frampton, W.J., Dash, J., Watmough, G.R., Milton, E.J.: Evaluating the capabilities of Sentinel-2 for quantitative estimation of biophysical variables in vegetation. ISPRS J. Photogramm. Remote Sens. 82, 83–92 (2013). https://doi.org/10.1016/j.isprsjprs.2013.04.007

Hu, J.F., Huang, T.Z., Deng, L.J., Jiang, T.X., Vivone, G., Chanussot, J.: Hyperspectral image super-resolution via deep spatiospectral attention convolutional neural networks. IEEE Trans. Neural Netw. Learn. Syst. 33(12), 7251–7265 (2022). https://doi.org/10.1109/TNNLS.2021.3084682

Jiang, J., Sun, H., Liu, X., Ma, J.: Learning spatial-spectral prior for super-resolution of hyperspectral imagery. IEEE Trans. Comput. Imaging 6, 1082–1096 (2020).

Kuenzer, C., Bluemel, A., Gebhardt, S., Quoc, T.V., Dech, S.: Remote sensing of mangrove ecosystems: A review. Remote Sens. 3(5), 878–928 (2011). https://doi.org/10.3390/rs3050878

Lassalle, G., Ferreira, M.P., La Rosa, L.E.C., Scafutto, R.D.P.M., de Souza Filho, C.R.: Advances in multi- and hyperspectral remote sensing of mangrove species: A synthesis and study case on airborne and multisource spaceborne imagery. ISPRS J. Photogramm. Remote Sens. 195, 298–312 (2023). https://doi.org/10.1016/j.isprsjprs.2022.12.003

McCarthy, M.J., Jessen, B., Barry, M.J., Figueroa, M., McIntosh, J., Murray, T., Schmid, J., Muller-Karger, F.E.: Automated high-resolution time series mapping of mangrove forests damaged by Hurricane Irma in Southwest Florida. Remote Sens. 12(11), 1740 (2020). https://doi.org/10.3390/rs12111740

Mondal, P., Dutta, T., Qadir, A., Sharma, S.: Radar and optical remote sensing for near real-time assessments of cyclone impacts on coastal ecosystems. Remote Sens. Ecol. Conserv. 8(4), 506–520 (2022). https://doi.org/10.1002/rse2.257

Sunkur, R., Kantamaneni, K., Bokhoree, C., Rathnayake, U., Fernando, M.: Mangrove mapping and monitoring using remote sensing techniques towards climate change resilience. Sci. Rep. 14, 6949 (2024). https://doi.org/10.1038/s41598-024-57563-4

Undrajavarapu, J., Sekhar, M.C.: Hyper spectral remote sensing for mapping species and characteristics of mangroves in Krishna Delta Region. Curr. World Environ. 15(3), 613–618 (2020). https://doi.org/10.12944/CWE.15.3.25

Wang, L., Jia, M., Yin, D., Tian, J.: A review of remote sensing for mangrove forests: 1956–2018. Remote Sens. Environ. 231, 111223 (2019). https://doi.org/10.1016/j.rse.2019.111223

Yokoya, N., Grohnfeldt, C., Chanussot, J.: Hyperspectral and multispectral data fusion: A comparative review of the recent literature. IEEE Geosci. Remote Sens. Mag. 5(2), 29–56 (2017). https://doi.org/10.1109/MGRS.2016.2637824

Zhang, et al.: [Reference corresponding to the Zhang et al. (2024) citation in the manuscript].